



HAL
open science

Molecular simulation of binary phase diagrams from the osmotic equilibrium method: vapour pressure and activity in water–ethanol mixtures

Michael Bley, Magali Duvail, Philippe Guilbaud, Christophe Penisson, Johannes Theisen, Jean Christophe Gabriel, Jean-François Dufrêche

► To cite this version:

Michael Bley, Magali Duvail, Philippe Guilbaud, Christophe Penisson, Johannes Theisen, et al.. Molecular simulation of binary phase diagrams from the osmotic equilibrium method: vapour pressure and activity in water–ethanol mixtures. *Molecular Physics*, 2018, 116 (15-16), pp.2009-2021. 10.1080/00268976.2018.1444209 . cea-01760168

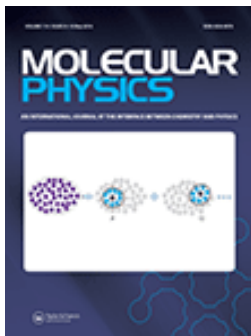
HAL Id: cea-01760168

<https://cea.hal.science/cea-01760168>

Submitted on 6 Apr 2018

HAL is a multi-disciplinary open access archive for the deposit and dissemination of scientific research documents, whether they are published or not. The documents may come from teaching and research institutions in France or abroad, or from public or private research centers.

L'archive ouverte pluridisciplinaire **HAL**, est destinée au dépôt et à la diffusion de documents scientifiques de niveau recherche, publiés ou non, émanant des établissements d'enseignement et de recherche français ou étrangers, des laboratoires publics ou privés.



Molecular simulation of binary phase diagrams from the osmotic equilibrium method: vapour pressure and activity in water–ethanol mixtures

Michael Bley, Magali Duvail, Philippe Guilbaud, Christophe Penisson, Johannes Theisen, Jean-Christophe Gabriel & Jean-François Dufrêche

To cite this article: Michael Bley, Magali Duvail, Philippe Guilbaud, Christophe Penisson, Johannes Theisen, Jean-Christophe Gabriel & Jean-François Dufrêche (2018): Molecular simulation of binary phase diagrams from the osmotic equilibrium method: vapour pressure and activity in water–ethanol mixtures, *Molecular Physics*, DOI: [10.1080/00268976.2018.1444209](https://doi.org/10.1080/00268976.2018.1444209)

To link to this article: <https://doi.org/10.1080/00268976.2018.1444209>



© 2018 The Author(s). Published by Informa UK Limited, trading as Taylor & Francis Group



[View supplementary material](#)



Published online: 13 Mar 2018.



[Submit your article to this journal](#)



Article views: 4



[View related articles](#)



[View Crossmark data](#)

Molecular simulation of binary phase diagrams from the osmotic equilibrium method: vapour pressure and activity in water–ethanol mixtures

Michael Bley^a, Magali Duval^a, Philippe Guilbaud^b, Christophe Penisson^c, Johannes Theisen^c, Jean-Christophe Gabriel^d and Jean-François Dufrêche^a

^aInstitut de Chimie Séparative de Marcoule (ICSM), UMR 5257, CEA, Université Montpellier, CNRS, Bagnols-sur-Cèze, France; ^bNuclear Energy Division, Research Department on Mining and Fuel Recycling Processes (SPDS/LILA), CEA, Bagnols-sur-Cèze, France; ^cInstitut de Chimie Séparative de Marcoule (ICSM), UMR 5257, CEA, Université Montpellier, CNRS, ENSCM, CEA Grenoble, Grenoble, France; ^dFundamental Research Division (DRF), CEA Grenoble, Grenoble, France

ABSTRACT

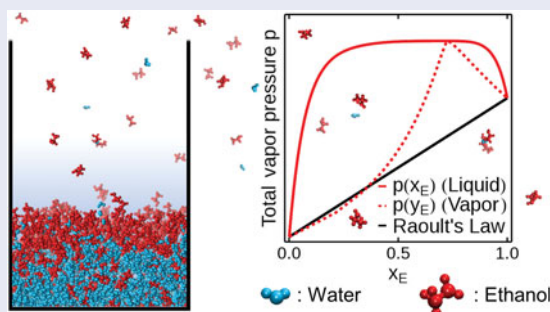
Herein, an approach for simulating phase diagrams of binary mixtures is presented, where a bulk liquid and its corresponding vapour phase are simulated by means of molecular dynamics using explicit polarisation. Time-averaged density profiles for the pure compounds and mixtures at different mole fractions provide information about the spatial distribution in the bulk liquid and the amount of evaporated species in the adjacent vapour phase. The activities in the liquid phase are calculated from the mean vapour phase densities at a given composition, providing a good qualitative agreement compared to experimental data and the precision of the method follows a previously developed Poisson model of evaporation. With the Redlich–Kister approach for the activities in a binary mixture, the directly obtained activities are fitted providing corrected activity coefficients of the two species. This method is applied to ethanol water mixtures at different mole fractions. The obtained structural data are in good agreement with experimental data and time-averaged density profiles provide a detailed insight into the composition of the liquid–vapour interface. An azeotropic point is obtained for an excess concentration of ethanol at 87% as percentage by mass compared to the experimental value of 95%.

ARTICLE HISTORY

Received 19 December 2017
Accepted 7 February 2018

KEYWORDS

Molecular dynamics;
vapour–liquid equilibria;
binary mixture; azeotrope;
activity coefficient




1. Introduction

The prediction of binary phase diagrams from molecular simulations is still a difficult challenge despite the significance of such an important concept. For example, since the early ages, mixtures of ethanol ($\text{CH}_3\text{CH}_2\text{OH}$) and water had a remarkable influence on human culture [1,2]. Almost all commercially available alcoholic beverages consist of a certain degree of ethanol and water. And when it comes to distilled beverages, physical chemistry comes into play. Distillation exploits the different

volatilities of compounds in a mixture, which, for example, allows separating ethanol from water due to the composition differences in the liquid mixture and its vapour phase. However, distillation only works, when the composition of the gas and the liquid phase differ. If compositions in gas and in the liquid are the same, then no further separation of the two compounds is possible, since the resulting distillate has the same composition as the initial liquid. This behaviour is called an azeotrope and for ethanol–water mixtures an azeotropic point is experimentally observed at 95.5 wt% of ethanol [3].

CONTACT Michael Bley  michaelbley@outlook.com; Jean-François Dufrêche  francois.dufreche@icsm.fr

 Supplemental data for this article can be accessed at <https://doi.org/10.1080/00268976.2018.1444209>.

© 2018 The Author(s). Published by Informa UK Limited, trading as Taylor & Francis Group

This is an Open Access article distributed under the terms of the Creative Commons Attribution-NonCommercial-NoDerivatives License (<http://creativecommons.org/licenses/by-nc-nd/4.0/>), which permits non-commercial re-use, distribution, and reproduction in any medium, provided the original work is properly cited, and is not altered, transformed, or built upon in any way.

Understanding the phase diagram for ethanol and water is thus of crucial importance for various industrial applications due to their relatively eco-friendly properties as solvent mixtures [4].

The latter is advantageous since ethanol allows solubilising compounds which are otherwise only poorly soluble in water, such as fragrance molecules in perfumes [5], longer aliphatic chained alcohols such as *n*-octanol for so-called surfactant free microemulsions [6,7], or many organic molecules such as peptides or active compounds in pharmaceuticals [8]. The increased solubility of non-polar compounds in these systems is due to the amphiphilic or surfactant-like character of the ethanol. The hydroxyl group of alcohols prefers the presence of polar compounds such as water and forms hydrogen bonds, whereas the short hydrocarbon chain prefers non-polar environments due to its hydrophobic nature [9] and consequently facilitates solubilising bigger, non-polar compounds. These properties make aqueous ethanol solutions elementary model systems before studying more complex solvent phases containing bigger amphiphilic molecules. The latter is for example used in solvent extraction systems for the treatment of spent nuclear fuels [10] or for recycling rare earth elements [11]. For process modelling of solvent extraction, knowing the activities in the liquid of all compounds is crucial to determine the efficiency of separation [12].

At equilibrium, the activity in the liquid phase of a compound in a mixture depends on the partial vapour pressure. Raoult's law describes the partial vapour pressure for ideal mixtures, where the partial vapour pressure is the product of the mole fraction and the vapour pressure of the pure liquid of that compound. Experimentally, activities of ethanol–water mixtures can be accessed by various methods. Barr-David and Dodge [13] and d'Ávila and Silva [14] measured the total vapour pressure for known compositions of the liquid and gas for different temperatures. O'Hare and Spedding [15] measured the evaporation rates of aqueous ethanol solutions under conditions of turbulent air flow. And more recently, Kokoric *et al.* [16] used substrate-integrated hollow waveguide infrared spectroscopy with integrated microfluidics to determine the partial pressure of ethanol and water. From a simulation perspective, Gibbs Ensemble Monte Carlo (GEMC) is capable in predicting vapour–liquid equilibria of binary mixtures in good agreement with experiment [17–20]. Lísal *et al.* [21] used the GEMC approach to simulate vapour–liquid equilibria of ethanol and water at 393.15 K. Other simulation methods for activities in solution, such as the molecular dynamics (MD) -based osmotic membrane method [22,23] or the McMillan–Mayer approach [24–26] only work for systems with charged particles. Zhang and Yang

[27], Noskov *et al.* [28] and more recently Ghoufi *et al.* [29] studied the structural and physical properties of aqueous ethanol–water mixtures in the bulk liquid phase and at the liquid–vapour interface by the means of MD simulation.

Herein, an extension of the previously presented osmotic equilibrium method [30] for binary solvent mixtures is presented. The method considers a vapour–liquid equilibrium for aqueous ethanol solutions between the liquid and its adjacent vapour phase. This method determines the average amount of molecules in the gas phase in analogy with the experimental studies of evaporation rates by O'Hare and Spedding [15]. This multi-scale approach based on the thermodynamic interpretation of the time-averaged density profiles from MD simulations of vapour–liquid interfaces is in principle similar to the experimental isopiestic approach for aqueous solutions. MD simulations of the bulk liquid phase and the liquid–vapour interfaces of ethanol–water mixtures have been conducted at different ethanol concentrations. Information about the osmotic properties of mixtures are consequently obtained by referring their vapour phase densities to those of the pure compounds. The methodological error, time-averaged density profiles, the coordination of the two species and the determination of an azeotrope are taken into account to show the extended scope of this approach.

2. Theoretical methods

2.1. Determination of activities from osmotic equilibria

For a binary mixture consisting of compounds 1 and 2 at mole fraction x_1 , the activity for the α th compound in the liquid phase in equilibrium with a vapour phase reads:

$$a_\alpha(x_1) = \frac{p_\alpha(x_1)}{p_\alpha^*} = \frac{n_\alpha(x_1)}{n_\alpha^*} = \frac{\rho_\alpha(x_1)}{\rho_\alpha^*} \quad (1)$$

where $p_\alpha(x_1)$, $n_\alpha(x_1)$ and $\rho_\alpha(x_1)$ are the vapour pressures, number densities and mass densities in the gas phase in equilibrium with the liquid for a composition x_1 . p_α^* , n_α^* and ρ_α^* are the vapour pressure, the number density and the mass density in the gas phase in equilibrium with the pure liquid α . The expressions represent the equilibrium between species in the liquid phase and species in a corresponding vapour phase. The non-ideal behaviour of the activity of a compound α in a liquid mixture at a composition x_1 can be described by the activity coefficient

$$\gamma_\alpha(x_\alpha) = \frac{\rho_\alpha(x_\alpha)}{x_\alpha \rho_\alpha^*} = \frac{a_\alpha(x_\alpha)}{x_\alpha} \quad (2)$$

which depends on the concentration.

2.2. Error calculation

A Poisson model helps understanding the error of the simulation method. The statistics of evaporation are discussed in detail in a previous publication [30]. The expected average amount of molecules of a species α found in the vapour phase $\bar{N}_\alpha(x_1)$ is

$$\bar{N}_\alpha(x_1) = \tau_\alpha \lambda_\alpha(x_1) \quad (3)$$

where $\lambda_\alpha(x_1)$ is the concentration-dependent evaporation rate and τ_α is the mean residence time in the gas phase. The mean residence time of a species τ_α is obtained through a Maxwell–Boltzmann distribution in the x direction:

$$\tau_\alpha = l_x \sqrt{\frac{\pi M_\alpha}{2RT}} \quad (4)$$

where l_x is the total length of the gas phase in x direction, M_α is the molar mass of the species, R is the ideal gas constant and T is the temperature. The activity of a compound in the liquid phase $a_\alpha(x_1)$ can be expressed as a fraction of evaporation rates by

$$a_\alpha(x_1) = \frac{\bar{N}_\alpha(x_1)}{\bar{N}_\alpha^*} = \frac{\lambda_\alpha(x_1)}{\lambda_\alpha^*} \quad (5)$$

where N_α^* and λ_α^* represent the amount of species and its corresponding evaporation rate for a pure liquid phase of a species α , respectively. The relative error of the expected amount of solvent molecules in the vapour phase $\delta_{\bar{N}_\alpha}(x_1)$ is calculated from a Poisson process [30]

$$\delta_{\bar{N}_\alpha}(x_1) = \frac{\Delta \bar{N}_\alpha(x_1)}{\bar{N}_\alpha(x_1)} = \frac{1}{\sqrt{\lambda_\alpha(x_1) t_p}} \quad (6)$$

where $\Delta \bar{N}_\alpha(x_1)$ is the total error for the quantity of a species found in the vapour phase and t_p is the total production time in the NVT ensemble. The production time t_p is given by

$$t_p = t_{\text{Tot}} - t_{\text{Eq}} \quad (7)$$

where t_{Tot} is the total simulation time and t_{Eq} is the time needed to equilibrate the system. The corresponding relative error of the activity of the liquid $\delta_{a_\alpha}(x_1)$ is

$$\begin{aligned} \delta_{a_\alpha}(x_\alpha) &= \frac{\Delta a_\alpha(x_1)}{a_\alpha(x_1)} = \frac{1}{\sqrt{t_p}} \left(\frac{1}{\sqrt{\lambda_\alpha(x_1)}} + \frac{1}{\sqrt{\lambda_\alpha^*}} \right) \\ &= \sqrt{\frac{\tau_\alpha}{t_p}} \left(\frac{1}{\sqrt{\bar{N}_\alpha(x_1)}} + \frac{1}{\sqrt{\bar{N}_\alpha^*}} \right) \end{aligned} \quad (8)$$

where $\Delta a_\alpha(x_1)$ is the total error of the activity. The latter can globally be calculated via

$$\Delta a_\alpha(x_1) = \sqrt{\frac{\tau_\alpha}{t_p}} \left(\frac{\sqrt{\bar{N}_\alpha(x_1)}}{\bar{N}_\alpha^*} + \frac{\bar{N}_\alpha(x_1)}{(\bar{N}_\alpha^*)^{3/2}} \right). \quad (9)$$

The resulting total error of the activity coefficient $\Delta \gamma_\alpha(x_\alpha)$ is

$$\Delta \gamma_\alpha(x_\alpha) = \frac{\Delta a_\alpha(x_\alpha)}{x_\alpha}. \quad (10)$$

It should be noted here that the mole fraction of the compound x_α is used instead of x_1 . The relative error of the activity coefficient $\delta_{\gamma_\alpha}(x_1)$ is equal to the relative error of the activity $\delta_{a_\alpha}(x_1)$. However, this is not true for the total errors $\Delta a_\alpha(x_1)$ and $\Delta \gamma_\alpha(x_\alpha)$. The error of the method is consequence of the variation for the amount of molecules present in the gas phase. In the case of an infinite trajectory length t_s the error will be zero.

3. Simulation details

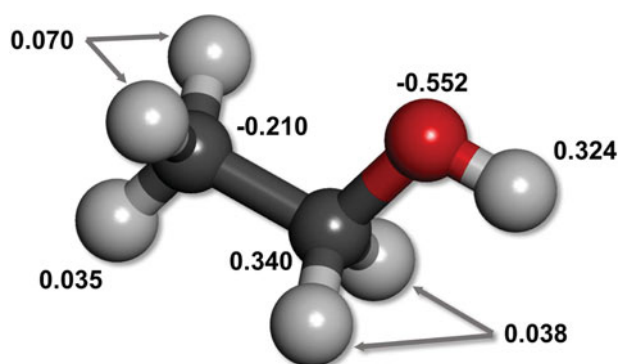
3.1. Molecular dynamics

Classical MD simulations of pure water, pure ethanol and their mixtures at different ethanol mole fractions x_E ranging from 0.1 to 0.9 were carried out with SANDER14, a module of AMBER14 [31], using explicit polarisation in the NPT and NVT ensembles. Periodic boundary conditions were applied to the simulation box in all directions. Equations of motion were numerically integrated using a 1.0 fs time step and long-range interactions have been calculated using the particle-mesh Ewald method [32]. Systems were equilibrated at 298.15 K and 1 bar (0.1 MPa) for 10 ns in the NPT ensemble, and production runs were afterwards conducted in the NVT ensemble for at least 15 ns. All atomic coordinates were written to the trajectory file every picosecond. Here, the van der Waals energy is described by a 12–6 Lennard-Jones potential. Water molecules were described by the rigid POL3 model [33,34], taking into account polarisation. The polarisable parm99 AMBER force field [35] was used to model the ethanol molecule (Table 1). Atomic partial charges on the ethanol were calculated using the restricted electrostatic potential procedure [36,37]. The atomic charges of the individual atoms are depicted in Figure 1. These sets of parameters provide a reasonable agreement of experimental [38] ($\rho_{\text{Exp.}} = 0.786 \text{ g cm}^{-3}$) and calculated density ($\rho_{\text{Sim.}} = 0.760 \text{ g cm}^{-3}$) for pure ethanol at 298.15 K.

Table 2 lists the initial ethanol mole fractions $x_{E, \text{ini}}$ and the dimensions of the simulation boxes created with the PACKMOL package [39]. The equilibration stage was

Table 1. Parameters used for the MD simulations.

Atom	$\epsilon_{\alpha\beta}$ ^a	$\sigma_{\alpha\beta}$ ^b	q_{α} ^c	α^d
O _{EtOH}	0.2104	3.060	-0.552	0.465
C _{EtOH} ^e	3.400	3.400	see Figure 1	0.878
H _{EtOH} ^e	-	-	+0.324	0.135
H _{EtOH} ^f	0.0157	2.650	see Figure 1	0.135
O _{H₂O}	0.665	3.204	-0.730	0.528
H _{H₂O}	-	-	+0.365	0.170

^aEnergies in kJ mol⁻¹.^bDistances in Å.^cAtomic partial charges in e.^dAtomic polarisabilities in Å³.^eHydrogen of hydroxyl group.^fHydrogen bound to carbon.**Figure 1.** Atomic partial charges of the ethanol molecule (in e) used for molecular dynamics simulations.

conducted for 8 to 10 ns in the *NPT* ensemble at 298.15 K and 1.0 bar using a τ_P of 0.1 ps, where τ_P is the relaxation time of the Berendsen pressure coupling [40]. Multiple production runs have been performed by changing the initial coordinates. For all simulation boxes of ethanol-water mixtures, three different equilibrated coordinate files of an identical composition have been used for each

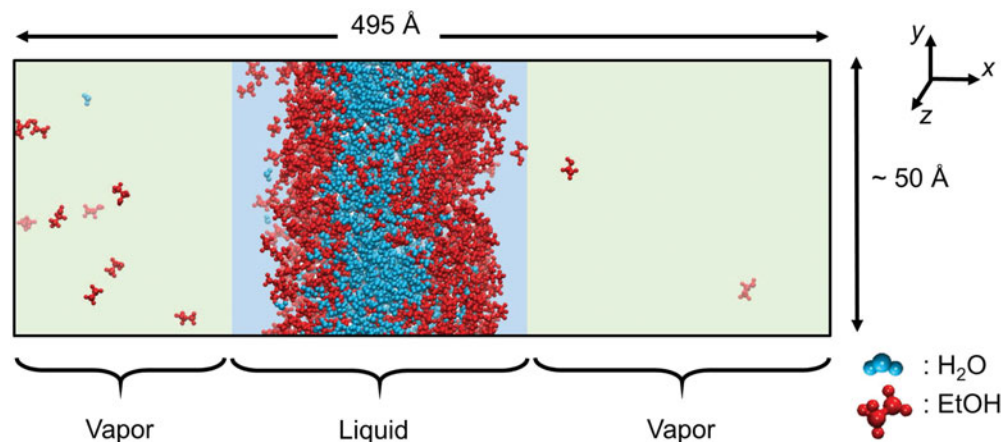
Table 2. Characteristics of the MD simulation boxes in the *NPT* ensemble.

$x_{E,ini}$ ^a	N_W ^b	N_E ^c	ρ_{Sim} ^d	ρ_{Exp} ^e	V_{Bulk} ^f
0	3300	-	0.996	0.997	$50.3 \times 50.3 \times 50.4$
0.1	2475	275	0.953	0.967	$52.8 \times 51.8 \times 51.9$
0.2	1886	471	0.908	0.939	$52.7 \times 52.9 \times 52.8$
0.3	1444	619	0.871	0.912	$52.9 \times 53.0 \times 52.1$
0.4	1100	733	0.845	0.889	$53.4 \times 53.0 \times 53.4$
0.5	825	825	0.824	0.869	$53.1 \times 53.3 \times 53.2$
0.6	600	900	0.809	0.852	$53.8 \times 53.8 \times 53.3$
0.7	412	962	0.792	0.838	$53.7 \times 54.2 \times 53.4$
0.8	254	1015	0.780	0.823	$53.6 \times 53.9 \times 53.9$
0.9	118	1061	0.770	0.807	$53.7 \times 53.8 \times 53.8$
1.0	-	1100	0.760	0.786	$53.9 \times 54.2 \times 53.8$

^aInitial ethanol mole fraction.^bNumber of water molecules.^cNumber of ethanol molecules.^dLiquid density in g cm⁻³ calculated from MD simulations in the *NPT* ensemble.^eExperimental liquid density in g cm⁻³ from Reference [38].^fLiquid bulk volume ($l_x \times l_y \times l_z$) in Å³.

mole fraction in order to ensure a good sampling. For the pure compounds, five different runs based on different initial coordinate files have been conducted.

Subsequently, simulation boxes have been extended to a finite size of 495.0 Å in *x*-direction to obtain liquid-vapour interfaces leading to a centred equilibrated bulk liquid phase and two adjacent vacuum areas with a width of around 225 Å each (Figure 2). Note that this vacuum space will hereafter be referred as the vapour phase. Similar partitioning between liquid and gaseous phases is found in the work of Taylor *et al.* [41], Yuet and Blankschtein [42] and Ghoufi *et al.* [29]. These geometries are used to produce liquid-vapour equilibria in the *NVT* ensemble for 15.0 ns at 298.15 K. The cut-off radius for all equilibration and production runs is 12.0 Å.

**Figure 2.** Schematic representation of a simulation box presenting an ethanol-water bulk liquid phase ($x_{E,ini} = 0.3$) in equilibrium with the adjacent vapour phase.

3.2. Data analysis

3.2.1. Time-averaged amount of molecules in the vapour phase

Data analysis has been performed using 37 production runs (Table 2). Equilibrium between the liquid and the vapour phase is obtained after around 8 ns for each production run, therefore only the results of the remaining 7.0 ns are taken into account for calculating the time-averaged amount of evaporated molecules $\langle N_{\alpha,i}(x_1) \rangle$ of a species α at a concentration x_1 during the i th run. The determination of the amount of molecules of type α present in the gas phase for a single frame $N_{\alpha,i}(t, x_1)$ requires the locations of both liquid–vapour interfacial yz -planes perpendicular to the x -axis. The latter are therefore located at 200 and 295 Å in x -direction, providing two gas phases of identical volume. All oxygen atoms of water molecules ($\text{O}_{\text{H}_2\text{O}}$) within the defined range from 0 to 200.0 and 295.0 to 495.0 Å are counted for each of the 7×10^3 frames of a trajectory and the arithmetic mean is calculated. Time-averaged density profiles for ethanol and water of the production runs are obtained from the coordinate files by calculating the arithmetic mean of a given compound for every 20th frame of a trajectory within an interval of 1.0 Å.

3.2.2. Determination of mean activities

The time-averaged amount of molecules $\langle N_{\alpha,i}(x_1) \rangle$ for a composition x_1 and the i th production run of a species α is calculated by

$$\langle N_{\alpha,i}(x_1) \rangle = \frac{1}{t_p} \int_{t_{\text{Eq}}}^{t_{\text{Tot}}} N_{\alpha,i}(t, x_1) dt \quad (11)$$

where $N_{\alpha}(t, x_1)$ is the amount of molecules α present in the gas phase at a simulation time t of the i th simulation run at a mole fraction x_1 . Here, the equilibration time t_{Eq} from Equation (7) is set to 7 ns. For a global simulation length t_{Tot} of 15 ns, the analysed production time t_p is therefore of 8 ns.

The amount of molecules in the gas phase is obtained for slightly different gas phase volumes for each run i . The volume of the gas phase varies because of the slightly different initial atomic coordinate files. The vapour phase density $\rho_{\alpha,i}(x_1)$ provides a volume-independent measure for the amount of evaporated molecules

$$\rho_{\alpha,i}(x_1) = \langle N_{\alpha,i}(x_1) \rangle \frac{M_{\alpha}}{V_i(x_1) N_A} \quad (12)$$

where M_{α} is the molar mass of compound α , N_A is the Avogadro constant and $V_i(x_1)$ is the total vapour phase volume of the i th run at a given concentration. The mean vapour phase density $\bar{\rho}_{\alpha}(x_1)$ of a species α is given by the

arithmetic mean of all j different runs

$$\begin{aligned} \bar{\rho}_{\alpha}(x_1) &= \frac{\sum_{i=1}^{j} \rho_{\alpha,i}(x_1)}{j} \quad \text{and} \\ \sigma_{\bar{\rho}_{\alpha}}(x_1) &= \frac{\sum_{i=1}^{j} \sigma_{\rho_{\alpha,i}}(x_1)}{j} \end{aligned} \quad (13)$$

where $x_1 = 0$ provides the vapour pressure of the pure species $\bar{\rho}_2^*$ and $x_1 = 1$ provides $\bar{\rho}_1^*$, respectively. The activity in the liquid phase $a_{\alpha}(x_1)$ is given by

$$a_{\alpha}(x_1) = \frac{\bar{\rho}_{\alpha}(x_1)}{\bar{\rho}_{\alpha}^*} \quad (14)$$

where $\bar{\rho}_{\alpha}^*$ is the vapour phase mass density of the pure components. The expressions for calculating the variation of the activity of a compound in the liquid phase are provided in the Appendix.

3.2.3. Fitting activities

Liquid phase activities and activity coefficients were fitted by using the Redlich–Kister equations as a function of the mole fraction [43]. For a binary mixture of a composition x_{α} , activities read:

$$\begin{aligned} a_{1,\text{act.}}(x_1) &= x_1 \exp \left[(1 - x_1)^2 [B + C(4x_1 - 1) \right. \\ &\quad \left. + D(2x_1 - 1)(6x_1 - 1)] \right] \end{aligned} \quad (15)$$

$$\begin{aligned} a_{2,\text{act.}}(x_1) &= (1 - x_1) \exp \left[x_1^2 [B + C(4x_1 - 3) \right. \\ &\quad \left. + D(2x_1 - 1)(6x_1 - 5)] \right] \end{aligned} \quad (16)$$

where B , C and D are the Redlich–Kister fitting coefficients. Those coefficients are used to fit the directly obtained simulated ethanol activities for the liquid phase $a_{\text{E,dir}}$ with Equation (15). Subsequently, this allows calculating $a_{\text{E,act}}$ and $a_{\text{W,act}}$ via the Equations (15) and (16), respectively. The fact that both a_1 and a_2 depend on the same coefficients B , C and D is a consequence of the Gibbs–Duhem relations. In this article, $a_{\alpha,\text{dir}}$ represent liquid phase activities directly obtained from MD simulation and $a_{\alpha,\text{act}}$ cover activities obtained from the Equations (15) and (16).

3.2.4. Phase compositions in the liquid and vapour phases

The mole fraction of compound α in the gas phase $y_{\alpha}(x_{\alpha})$ for a non-ideal mixture varies with the composition of the liquid phase x_{α} . An azeotropic point is obtained if $x_{\alpha} = y_{\alpha}(x_{\alpha})$, where the composition is the same for both

phases. $y_1(x_1)$ for an ideal gas mixture is defined as

$$y_1(x_1) = \frac{N_{1,\text{gas}}(x_1)}{N_{1,\text{gas}}(x_1) + N_{2,\text{gas}}(x_1)} = \frac{p_1(x_1)}{p_1(x_1) + p_2(x_1)} \quad (17)$$

where $N_{\alpha,\text{gas}}(x_1)$ is the amount of a species α for a mole fraction x_1 in the gas phase and $p_{\alpha}(x_1)$ is the corresponding vapour pressure of the compound, respectively. Vapour pressures in the gas phase $p_{\alpha}(x_1)$ can be accessed by

$$p_{\alpha}(x_1) = a_{\alpha}(x_1)p_{\alpha}^* \quad (18)$$

4. Results and discussion

4.1. Liquid phase

Table 2 contains a comparison of experimental and calculated densities at different ethanol mole fractions. The calculated density of pure ethanol is in good agreement with experimental findings [38], whereas a certain mismatch is observed for the ethanol-water mixtures. For $x_E = 0.3$ and 0.8 , the difference is around 0.04 g cm^{-3} and this underestimation of the densities indicates that the ethanol-water intermolecular interactions might be too weak. Table 3 provides selected structural properties of two species in the bulk liquid phase for the simulation of a liquid-vapour interface in the *NVT* ensemble. The corresponding ethanol-ethanol distance $r_{\text{O}_E-\text{O}_E}$ of 2.85 \AA is consistent with previously obtained experimental [44] and simulated data [28,45,46]. Narten and

Habenschuss [44] showed by X-ray diffraction measurements of pure ethanol, that the distance between two hydroxyl groups is around 2.8 \AA and that 1.8 nearest neighbours are found at this distance. Our simulation yields a distance of 2.85 \AA and 1.6 nearest neighbours. For mixtures, only slight changes of first-order maximum peak position between water and ethanol are observed for an increasing concentration. The distances $r_{\text{O}_E-\text{O}_W}$ and $r_{\text{O}_E-\text{H}_W}$ increase by 0.02 \AA whereas distances for the same species remain constant ($r_{\text{O}_E-\text{O}_E}$, $r_{\text{H}_E-\text{H}_E}$, $r_{\text{O}_W-\text{O}_W}$ and $r_{\text{H}_W-\text{H}_W}$). The sum of the coordination numbers for the first-order maximum $\text{CN}_{\text{O}_E-\text{H}_2\text{O}}$ and $\text{CN}_{\text{O}_E-\text{O}_E}$ is between 1.6 and 1.8 for any composition. An increasing ethanol content leads to a replacement of water molecules by ethanol molecules in the first hydration sphere. This shows that the structural properties of the mixtures are very similar to those of the pure compounds. The plotted radial distribution functions (RDF) and coordination numbers (CN) as well as additional tables listing hydration properties for the *NPT* and the *NVT* ensemble are provided in the Supporting Information (Tables S1–S4 and Figures S1–S16).

Another aspect of the structural properties in the liquid phase is time-averaged mass density profiles from the simulations in the *NVT* ensemble of the liquid-vapour equilibrium. Figures 3–5 show anisotropies of the density in x and y direction of the two compounds with respect to the orientation of the liquid-vapour interface. Detailed time-averaged mass density profiles for studied mole fractions (*NVT* and *NPT* ensemble) are provided in the Supporting Information (Figures S17–S36). The density profiles in y direction parallel to the liquid-vapour interface

Table 3. Hydration properties of ethanol-water mixtures at 298.15 K calculated at different mole fractions in the *NVT* ensemble.

$x_{E,\text{ini.}}^a$	$r_{\text{O}_E-\text{O}_W}^b$	$r_{\text{O}_E-\text{H}_W}^c$	$\text{CN}_{\text{O}_E-\text{H}_2\text{O}}^d$	$r_{\text{O}_E-\text{O}_E}^e$	$\text{CN}_{\text{O}_E-\text{O}_E}^f$	$r_{\text{H}_E-\text{H}_E}^g$	$r_{\text{O}_W-\text{O}_W}^h$	$r_{\text{H}_W-\text{H}_W}^i$
0	–	–	–	–	–	–	2.74	1.64
0.1	2.80	1.82	1.30	2.85	0.45	2.55	2.74	1.64
0.2	2.81	1.82	1.04	2.85	0.69	2.55	2.75	1.63
0.3	2.81	1.82	0.85	2.85	0.88	2.56	2.74	1.63
0.4	2.81	1.82	0.73	2.85	1.00	2.55	2.74	1.64
0.5	2.81	1.82	0.62	2.84	1.10	2.56	2.74	1.63
0.6	2.81	1.82	0.52	2.85	1.19	2.56	2.74	1.63
0.7	2.81	1.82	0.46	2.85	1.25	2.55	2.75	1.63
0.8	2.81	1.84	0.34	2.85	1.35	2.56	2.75	1.64
0.9	2.82	1.84	0.20	2.85	1.48	2.55	2.75	1.64
1.0	–	–	–	2.85	1.62	2.57	–	–

^aInitial ethanol mole fraction.

^bFirst-order maximum peak of the $\text{O}_E - \text{O}_W$ RDF in \AA .

^cFirst-order maximum peak of the $\text{O}_E - \text{H}_W$ RDF in \AA .

^dNumber of water molecules in the first coordination sphere of O_E .

^eFirst-order maximum peak of the $\text{O}_E - \text{O}_E$ RDF in \AA .

^fNumber of O_E in the first coordination sphere of O_E .

^gFirst-order maximum peak of the $\text{H}_E - \text{O}_E$ RDF in \AA .

^hFirst-order maximum peak of the $\text{O}_E - \text{O}_W$ RDF in \AA .

ⁱFirst-order maximum peak of the $\text{H}_W - \text{O}_W$ RDF in \AA .

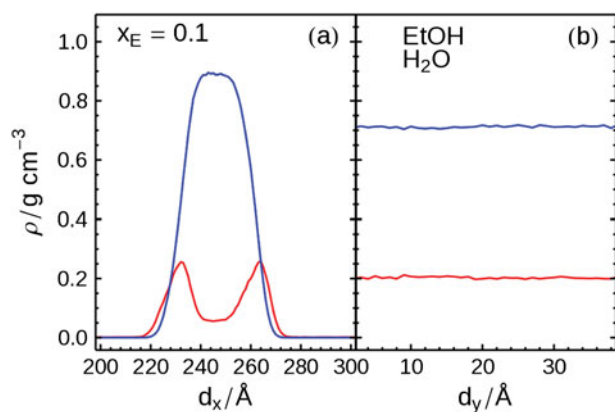


Figure 3. Time-averaged density profiles along the (a) x axis and (b) y axis for ethanol EtOH (dashed) and water H₂O (joined) at an ethanol mole fraction $x_E = 0.1$ in the NVT ensemble.

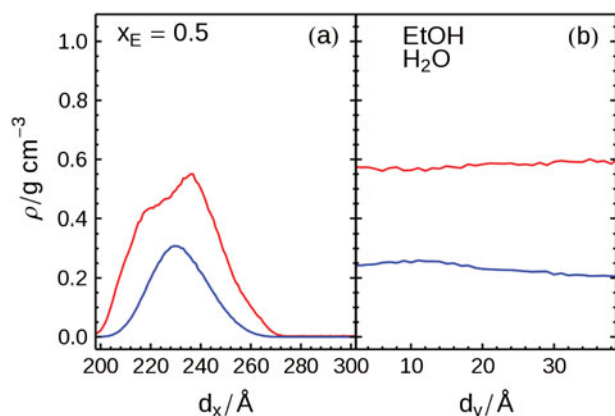


Figure 4. Time-averaged density profiles along the (a) x axis and (b) y axis for ethanol EtOH (dashed) and water H₂O (joined) at an ethanol mole fraction $x_E = 0.5$ in the NVT ensemble.

correspond to the behaviour of the bulk liquid because of the periodic conditions applied on the simulation boxes. In x direction, perpendicular to the interface, the presence of a vapour phase leads to an inhomogeneous distribution of molecules of the two species. Ethanol molecules accumulate at the liquid–vapour interface due to their more amphiphilic nature and the preferred orientation of their short hydrophobic alkyl chains is towards the non-polar vapour phase. Therefore, water molecules as a polar compound, tend to stay in the bulk liquid phase. The formation of interfacial layers of ethanol is observed for any ethanol content in the mixture, as it can be seen in the snapshots in Figure 6. The thickness of this layer increases with increasing ethanol content. Figure 6(b) shows that excess water is found on the left side of the bulk liquid phase, which might explain the asymmetric curve for ethanol in Figure 4.

It is necessary to take this effect into account for the composition of the bulk liquid phase. The ethanol mole fraction in the liquid $x_{E, \text{liq}}$ can be derived from

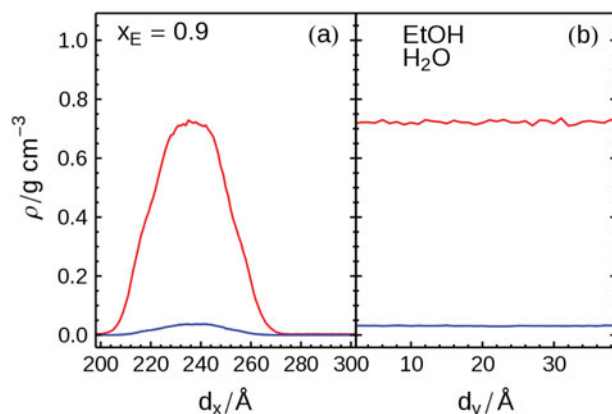


Figure 5. Time-averaged density profiles along the (a) x axis and (b) y axis for ethanol EtOH (dashed) and water H₂O (joined) at an ethanol mole fraction $x_E = 0.9$ in the NVT ensemble.

the time-averaged number density profiles. The liquid composition $x_{E, \text{liq}}$ is calculated by the number density in the middle of the box around the maximum water density in x direction by averaging over all points within ± 15 Å of this maximum. Indeed, only the central molecules of the liquid phase have a bulk environment that corresponds to the liquid phase concentration. Thus, the corrected ethanol mole fraction, as tabulated in Table 5, exhibits a negative offset of around 0.1 compared to the initial composition $x_{E, \text{ini}}$, indicating the depletion of ethanol molecules in the bulk liquid phase. A comparison of the anisotropy of the liquid phase composition in the x , y and z direction is part of the supporting information (Table S5 and Figure S37).

4.2. Vapour phase

The amount of molecules present in the vapour phase is a direct result of simulations in the NVT ensemble. Equation (3) consequently leads to the evaporation rate λ_α , which varies with the composition and depends on the residence time τ_α . For $l_x = 400.0$ Å, the mean residence times of ethanol and water are $\tau_E = 216.1$ ps and $\tau_W = 135.2$ ps, respectively. Total and relative errors of the method for the two species can then be accessed.

Table 4 lists the key parameters for the statistics of evaporation using a Poisson model [30]. The mean amount of ethanol \bar{N}_E increases up to 50 molecules with increasing ethanol content, whereas the amount of water in the gas phase \bar{N}_W remains almost constant at around 3. Consequently, the evaporation rate of ethanol λ_E is higher by up to a factor of 10 when compared to water. A higher evaporation rate for the same simulation length t_S thus leads to a reduced error following Equation (6). The relative error for ethanol δ_E and water δ_W differ by a factor ranging between 2 and 3, dependent on the initial

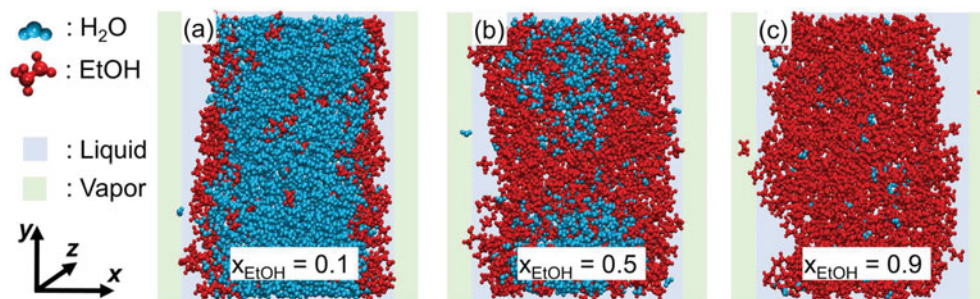


Figure 6. Parts of snapshots of the simulation boxes representing the liquid phase (darker background) in contact with the two vapour phases (brighter background) for an ethanol mole fraction of (a) 0.1, (b) 0.5 and (c) 0.9.

composition. The higher the ethanol content, the lower the relative error of the method δ_E . Similarly, the absolute error for the activity Δa_E is lower by a factor of 4 than for Δa_W .

In Table 4, activities a_α of the two species in the liquid phase are listed as well. For ethanol, a constant increase of activity is observed, whereas the water activity a_W remains constantly above 1.0 up to high ethanol concentration. This is in agreement with the vapour phase densities tabulated in Table 5, where $\rho_{W, \text{gas}}(x_1)$ permanently exceeds the vapour phase density of pure water. The presence of ethanol molecules leads to a drastic increase of water vapour phase densities. This behaviour can be explained by two observations. First, the formation of an interfacial ethanol layer hinders the evaporation of water molecules in the gas phase by forming a less permeable layer. This observation is supported by the fact that the water gas phase density remains almost constant for all different mixture compositions. Thus, the organisation of the interface hinders its evaporation and the

system is not fully equilibrated. This is a consequence of the lower amount of water at the interface induced by the amphiphilic and surfactant nature of ethanol. Second, the intermolecular interaction between the same and different species are too weak. These forces depend on the initially chosen atomic interaction parameters $\epsilon_{\alpha\beta}$. It should be noted that simulated vapour pressures of pure ethanol $p_{E, \text{sim.}}^* = 3.335$ bar and water $p_{W, \text{sim.}}^* = 0.091$ bar when compared to their experimental values $p_{E, \text{exp.}}^* = 0.079$ bar [47] and $p_{W, \text{exp.}}^* = 0.032$ bar [3] differ by factors of around 40 and 3, respectively. Stronger intermolecular interactions would result in lower vapour pressures of the pure compounds.

In addition, Table 5 contains variations σ for the vapour phase densities and the related activities. Compared to the error of the method for the activity Δa_α , the standard deviation of activities in the liquid phase σ_{a_α} show no concentration dependency. An increasing concentration does not lead to a decreasing variation. The globally lower amount of water molecules in the gas

Table 4. Statistics of evaporation for ethanol–water mixtures at 298.15 K.

$x_{E, \text{ini.}}^a$	\bar{N}_E^b	λ_E^c	$\delta_{\bar{N}_E}^d$	$a_E \pm \Delta a_E^e$	\bar{N}_W^f	λ_W^g	$\delta_{\bar{N}_W}^h$	$a_W \pm \Delta a_W^i$
0.0	–	–	–	0	2.6	0.019	8.6%	1.0
0.1	18.0	0.083	4.1%	0.416 ± 0.024	2.5	0.019	8.7%	1.152 ± 0.166
0.2	32.6	0.150	3.1%	0.721 ± 0.036	2.6	0.020	8.6%	1.152 ± 0.171
0.3	38.9	0.180	2.8%	0.839 ± 0.041	2.6	0.020	8.5%	1.128 ± 0.172
0.4	40.9	0.189	2.7%	0.858 ± 0.042	2.9	0.021	8.2%	1.182 ± 0.182
0.5	41.9	0.194	2.7%	0.864 ± 0.043	3.0	0.022	8.0%	1.231 ± 0.190
0.6	43.3	0.200	2.7%	0.887 ± 0.044	2.9	0.022	8.1%	1.180 ± 0.185
0.7	45.1	0.209	2.6%	0.903 ± 0.046	3.4	0.025	7.6%	1.330 ± 0.206
0.8	44.9	0.208	2.6%	0.909 ± 0.045	3.1	0.023	7.8%	1.258 ± 0.196
0.9	47.0	0.218	2.6%	0.935 ± 0.047	2.5	0.019	8.7%	0.994 ± 0.166
1.0	50.4	0.233	2.5%	1.0	–	–	–	0

^aInitial ethanol mole fraction.

^bMean time-averaged amount of ethanol in the vapour phase.

^cEthanol evaporation rate in ps^{-1} .

^dRelative error of the amount of ethanol in the vapour phase in %.

^eEthanol activity in the liquid phase and the corresponding error.

^fMean time-averaged amount of water in the vapour phase.

^gWater evaporation rate in ps^{-1} .

^hRelative error of the amount of water in the vapour phase in %.

ⁱWater activity in the liquid phase and the corresponding error.

Table 5. Raw gas-phase properties of ethanol–water mixtures simulated at 298.15K.

$x_{E,ini}^a$	$x_{E,liq}^b$	$\rho_{E,gas} \pm \sigma_{\rho_{E,gas}}^c$	$a_{E,liq} \pm \sigma_{a_{E,liq}}^d$	$\rho_{W,gas} \pm \sigma_{\rho_{W,gas}}^e$	$a_{W,liq} \pm \sigma_{a_{W,liq}}^f$
0.0	–	–	0	0.066 ± 0.007	1.0
0.1	0.04	1.382 ± 0.030	0.416 ± 0.013	0.076 ± 0.008	1.152 ± 0.223
0.2	0.13	2.404 ± 0.047	0.721 ± 0.022	0.076 ± 0.002	1.152 ± 0.133
0.3	0.17	2.798 ± 0.032	0.839 ± 0.018	0.075 ± 0.010	1.128 ± 0.252
0.4	0.25	2.860 ± 0.014	0.858 ± 0.013	0.078 ± 0.002	1.182 ± 0.138
0.5	0.39	2.883 ± 0.033	0.864 ± 0.019	0.081 ± 0.001	1.231 ± 0.131
0.6	0.45	2.957 ± 0.020	0.887 ± 0.015	0.078 ± 0.002	1.180 ± 0.136
0.7	0.58	3.011 ± 0.050	0.903 ± 0.025	0.088 ± 0.005	1.330 ± 0.202
0.8	0.72	3.032 ± 0.020	0.909 ± 0.016	0.083 ± 0.001	1.258 ± 0.137
0.9	0.83	3.118 ± 0.025	0.935 ± 0.017	0.066 ± 0.003	0.994 ± 0.131
1.0	–	3.335 ± 0.035	1.0	–	0

^aInitial ethanol mole fraction.

^bEthanol mole fraction in the liquid.

^cEthanol vapour phase mass density $\rho_{E,gas}$ and the corresponding standard deviation $\sigma_{\rho_{E,gas}}$ in g m^{-3} .

^dEthanol activity in the liquid phase $a_{E,gas}$ and the corresponding standard deviation $\sigma_{a_{E,gas}}$.

^eWater vapour phase mass density $\rho_{W,gas}$ and the corresponding standard deviation $\sigma_{\rho_{W,gas}}$ in g m^{-3} .

^fWater activity in the liquid phase $a_{W,gas}$ and the corresponding standard deviation $\sigma_{a_{W,gas}}$.

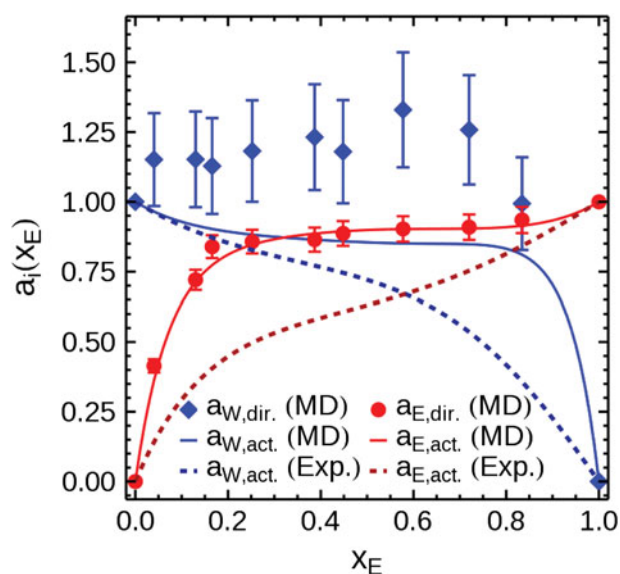


Figure 7. Simulated and experimental activities a_W and a_E in the liquid phase as a function of the ethanol mole fraction x_E . Experimental data from reference [14].

phase \bar{N}_W compared to \bar{N}_E is the reason why the standard deviation of the vapour phase density $\sigma_{\rho_{W,gas}}$ is lower and the variation of the activity of the liquid $\sigma_{a_{W,liq}}$ is higher compared to those of ethanol. For the water evaporation rate λ_W , O'Hare and Spedding [15] measured that the water evaporation rate remained virtually constant with increasing ethanol content.

Table 5 lists the initial $x_{E,ini}$ and corresponding liquid phase $x_{E,liq}$ mole fraction, where the latter is obtained from the time-averaged number density profiles in x direction. The composition of the liquid phase is used in Figure 7 to illustrate the behaviour of the liquid phase activities and their total errors $a_\alpha \pm \Delta a_\alpha$ for an

increasing ethanol concentration. Water activities a_W for mixtures are too high and they do not fulfil Raoult's law, as the vapour pressure of a pure compound is always required to be higher than its mixture. Ethanol activities a_E follow experimentally observed tendencies [14] with a reasonable total methodological error Δa_W .

4.3. Fitting the ethanol activities

Figure 7 shows the directly obtained activities for the liquid phase $a_{\alpha,dir.}$, the curves for $a_{\alpha,act.}$ from a Redlich–Kister fit of the ethanol activities calculated from MD and finally curves based on the Redlich–Kister parameters obtained from experiment [14]. Raw simulated ethanol activities $a_{E,dir.}$ have been fitted with Equation (15). Indeed, only ethanol activities have been chosen for fitting because of equilibration difficulties for water. Corresponding water activities obtained from Equation (16) that express the Gibbs–Duhem relation are also plotted. This provides $B_{Sim.} = 2.246$, $C_{Sim.} = 0.101$ and $D_{Sim.} = 0.321$. D'Ávila and Silva [14] obtained $B_{Exp.} = 1.196$, $C_{Exp.} = -0.267$ and $D_{Exp.} = -0.081$ for ethanol–water mixtures at 298.15 K via the total pressure method. For simulation results, Equation (16) allows to determine adjusted water activities $a_{W,act.}$ from the fit of the ethanol data. The two curves for $a_{\alpha,act.}$ from simulation still exceed the corresponding experimental findings, but no more activities above 1 is obtained and the modelled activities $a_{\alpha,act.}$ still predict a repulsive system.

Thus, the obtained curves for activities in the liquid phase $a_{\alpha,act.}$ can subsequently be used to calculate activity coefficients for solutes via Equation (2). Figure 8 allows comparing the results for fitting coefficients from both, simulation and experiment. Activity coefficients obtained from simulation are in general higher compared to

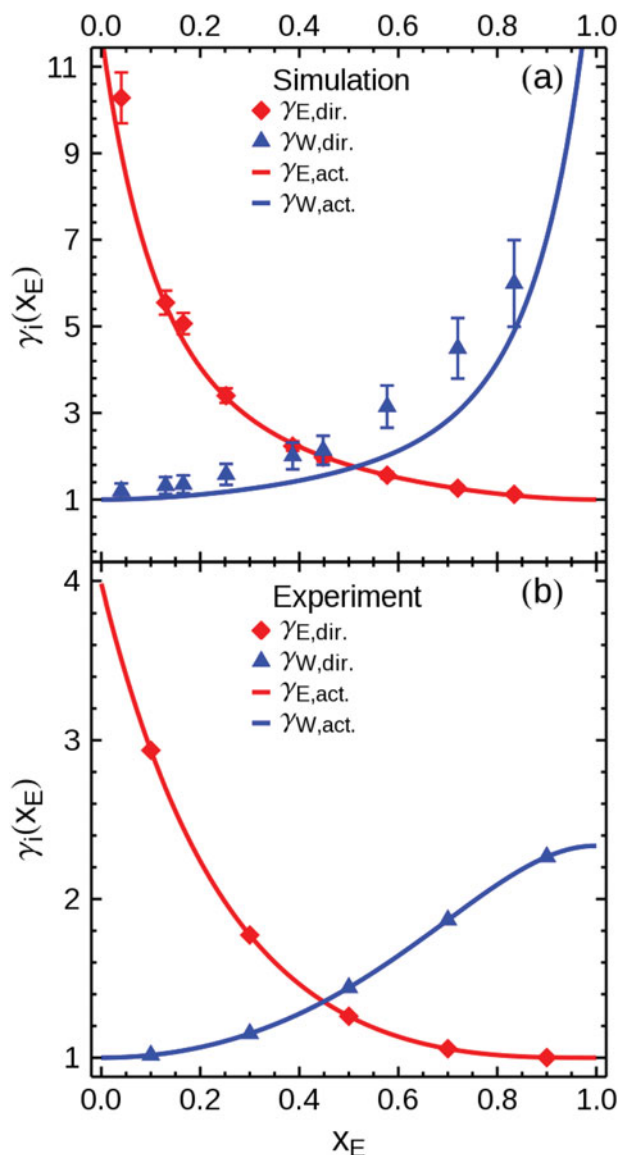


Figure 8. Raw and fitted water γ_W and ethanol γ_E activity coefficients as function of the ethanol mole fraction x_E . Experimental data from reference [14].

experimental ones, but general trends are observed. For water, the fact that simulation points do not fully correspond to the Redlich–Kister curve fitted from ethanol points is the consequence of the non-equilibration of water and the underestimation of intermolecular interactions. Thus, the Gibbs–Duhem equation is not satisfied and the points do not exactly coincide. Nevertheless, differences are not that big and it globally corresponds to the lower value of the error bar. Knowing the two activities $a_{E, \text{act.}}$ and $a_{W, \text{act.}}$ also allows tracing the partial vapour pressures of ethanol and water $p_\alpha(x_1)$ with the help of Equation (18) and a given vapour pressure of the pure compound p_α^* . Using experimental vapour pressures of pure ethanol $p_E^* = 0.079$ bar [47] and water $p_W^* = 0.032$ bar at 298.15K [3], allows comparing the outcome of

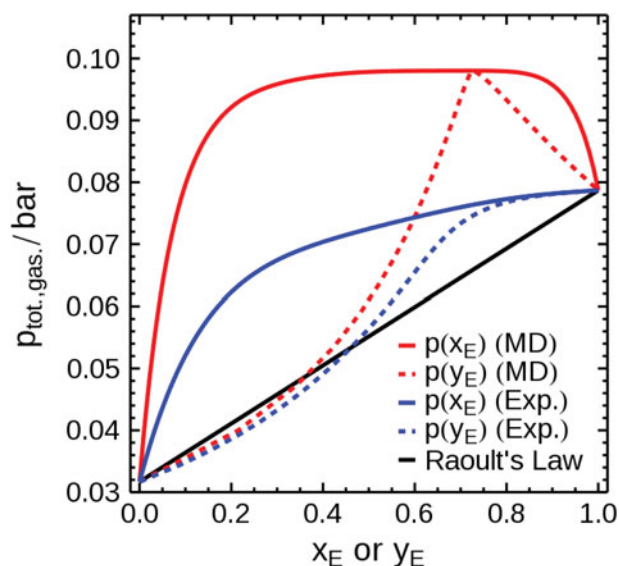


Figure 9. Total vapour pressure of the gas phase $p_{\text{tot., vap.}}$ as a function of the ethanol mole fraction in the liquid phase x_E and in the gas phase y_E , respectively. Experimental data from reference [14].

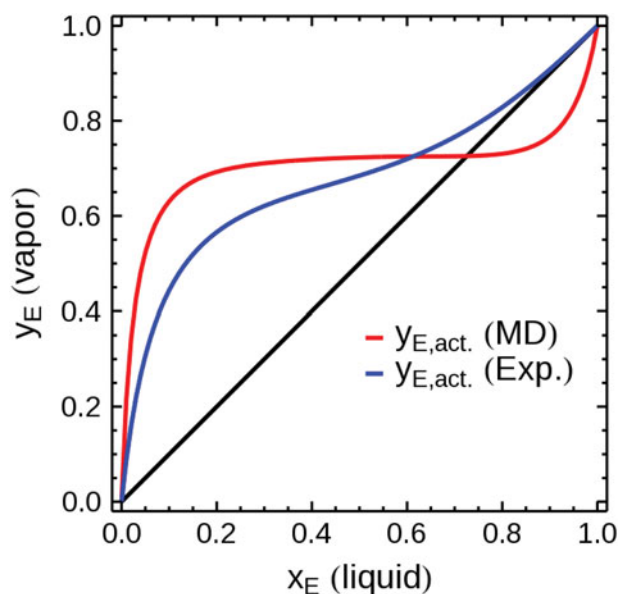


Figure 10. Ethanol mole fraction of the gas phase y_E as a function of the ethanol mole fraction in the bulk liquid phase x_E . The straight line corresponds to azeotropic behaviour, where $x_E = y_E$. Experimental data from reference [14].

simulation and experiment. The total vapour pressure $p_{\text{total}}^{\text{vapour}}$, as shown in Figure 9, is given by the sum of the partial vapour pressures p_E and p_W . The mole fraction of ethanol in the gas phase y_E in Figure 10 is calculated via Equation (17).

In Figure 9, the vapour pressure is plotted as a function of the ethanol content in the bulk liquid phase x_E (solid line) and the ethanol mole fraction in the gas phase y_E (dashed line) for calculated and experimental activities.

The vapour pressures as a function of the liquid phase composition x_E are calculated using Equation (18) using the fitted activities $a_{\alpha, \text{act}}$. The experimental vapour pressures p_{α}^* of the pure compounds are used here to compare simulation and experiment. Subsequently, Equation (17) allows determining the total vapour pressure as a function of the ethanol concentration in the gas phase y_E . For the liquid phase, a positive deviation from Raoult's law is observed indicating solute aggregation. Curves for the composition of vapour phase $p(y_E)$ almost follow Raoult's law for a low total ethanol content, but for composition higher than $x_E = 0.4$, the total vapour pressure as a function of y_E approaches the curve for the composition of the liquid until the azeotropic point. At the azeotropic point the composition of the liquid is the same as the composition in the gas phase. The azeotropic point experimentally observed is found at an ethanol mass fraction $w_E = 95.5\%$, which corresponds to $x_E = 0.89$ [3]. For the simulated data, the azeotropic point is found at $x_E = 0.73$, which equals 87 wt% of ethanol in the mixture. The model is therefore in agreement with experimental data, as it predicts an azeotropic mixture for an ethanol/water system, although at a slightly lower weight fraction of ethanol. The inversion of the phase composition for ethanol concentrations above the azeotropic composition can be observed for longer chain alcohol-water mixtures, such as in the propan-2-ol-water system [48].

In Figure 10, the solid black line corresponds to the azeotrope $x_E = y_E$ and the azeotropic composition of the simulated ethanol-water mixtures is found at the intersection with this line. For the experimental curves, the azeotrope is given by the composition where blue line overlaps the black line.

5. Conclusion

Liquid-vapour equilibria of ethanol-water mixtures at different ethanol mole fractions have been performed by means of MD simulations using explicit polarisation. Thermodynamic properties for two compounds such as their activity or their activity coefficient in the liquid phase were calculated and found to be in a reasonable agreement with experimental values [14] when fitting ethanol activities $a_{E, \text{dir}}$ with Redlich-Kister equations [43]. Polarisable force fields for ethanol and water allow reproducing the liquid phase densities again in good agreement with experiments [38], but provide higher vapour phase densities and consequently higher vapour pressure than observed experimentally. Analysis of time-averaged density profiles and of radial distribution functions provided structural information of the bulk liquid phase and its liquid-vapour interface. It has been

observed that even at a low ethanol mole fraction, ethanol molecules tend to accumulate at the liquid-vapour interface due to their amphiphilic properties. Furthermore, each ethanol molecule has between 1.6 to 1.8 water or ethanol molecules as their closest neighbour in the first coordination sphere at a ratio dependent on the mole fraction. In addition, it has been shown that the statistics of evaporation for both molecules at any composition can be described by a previously introduced Poisson model. The resulting amount of molecules in the gas phase and the corresponding activities of the two species in the liquid phase are higher than expected. This augmented pressure originates from too weak intermolecular interactions and the formation of an ethanol layer at the interface, which acts as a barrier for evaporation. Thus, the liquid-vapour equilibrium is not fully equilibrated. However, fitting ethanol activities directly obtained from simulations with the Redlich-Kister method associates the Gibbs-Duhem relation and allows accessing activity coefficients for the two compounds in the liquid phase. Thus, the obtained activities are used to determine the gas phase compositions and subsequently the total vapour pressure of the gas phase as a function of the compositions in different phases. This procedure measures an azeotropic point from simulation for a binary mixture. The azeotropic composition is around 87% (in mass fraction) relatively close to the experimental value of 95%.

The osmotic equilibrium method as described previously [30] can be extended on phase diagram simulations for binary mixtures. This method provides helpful tools for calculating activity coefficients and binary phase diagrams of mixtures. Furthermore, it should be kept in mind that the osmotic equilibrium method is based on a bottom-up multi-scale approach. This means that different force fields for the different species at an atomic or molecular scale will provide different results for the global thermodynamic properties. It has been shown that the method itself paves the way for future investigations for accessing phase diagrams and interfacial properties of a huge bandwidth of different mixtures such as the complex organic mixtures used in separation chemistry or even ones containing charged compounds.

Acknowledgments

This work was made possible, thanks to the high-performance computing facilities of TGCC/CCRT and the computing centre of CEA Marcoule.

Disclosure statement

No potential conflict of interest was reported by the authors.

Funding

The research leading to these results has received funding from the European Research Council under the European Union's Seventh Framework Programme [grant number FP/2007–2013]; ERC Grant Agreement [grant number 320915] 'RECYCLE': Rare Earth Element reCYCling with Low harmful Emissions.

ORCID

Michael Bley  <http://orcid.org/0000-0001-6559-4274>

Philippe Guilbaud  <http://orcid.org/0000-0001-9777-8326>

References

- [1] D. Cavalieri, P.E. McGovern, D.L. Hartl, R. Mortimer, and M. Polsinelli, *J. Mol. Evol.* **57**, 226–232 (2003). doi:10.1007/s00239-003-0031-2
- [2] P.E. McGovern, J. Zhang, J. Tang, Z. Zhang, G.R. Hall, R.A. Moreau, A. Nunez, E.D. Butrym, M.P. Richards, C.S. Wang, G. Cheng, Z. Zhao, and C. Wang, *Proc. Natl. Acad. Sci.* **101**(51), 17593–17598 (2004). doi:10.1073/pnas.0407921102
- [3] D.R. Lide, *CRC Handbook of Chemistry and Physics*, 85th ed. (CRC Press LLC, Boca Raton, FL, 2005).
- [4] C. Capello, U. Fischer, and K. Hungerbühler, *Green Chem.* **9**(9), 927–934 (2007). doi:10.1039/b617536h
- [5] J. Marcus, M.L. Klossek, D. Touraud, and W. Kunz, *Flavour Fragr. J.* **28**(5), 294–299 (2013). doi:10.1002/ffj.3172
- [6] M.L. Klossek, D. Touraud, T. Zemb, and W. Kunz, *Chem. Phys. Chem.* **13**(18), 4116–4119 (2012). doi:10.1002/cphc.201200667
- [7] S. Schöttl and D. Horinek, *Curr. Opin. Colloid Interface Sci.* **22**, 8–13 (2016).
- [8] A. Li and S.H. Yalkowsky, *J. Pharm. Sci.* **83**(12), 1735–1740 (1994). doi:10.1002/jps.2600831217
- [9] C. Tanford, *The Hydrophobic Effect: Formation of Micelles and Biological Membranes*, 2nd ed. (J. Wiley, New York, 1980).
- [10] B. Bonin, B. Bouquin, M. Dozol, M. Lecomte, and A. Forestier, *Treatment and Recycling of Spent Nuclear Fuel: Actinide Partitioning – Application to Waste Management* (CEA Saclay and Groupe Moniteur, Paris, 2008).
- [11] K. Binnemans, P. Tom, B. Blanpain, T.V. Gerven, Y. Yang, A. Walton, and M. Buchert, *J. Clean. Prod.* **51**, 1–22 (2013). doi:10.1016/j.jclepro.2012.12.037
- [12] M. Bley, B. Siboulet, A. Karmakar, T. Zemb, and J.F. Dufrêche, *J. Colloid Interface Sci.* **479**, 106–114 (2016). doi:10.1016/j.jcis.2016.06.044
- [13] F. Barr-David and B.F. Dodge, *J. Chem. Eng. Data* **4**(2), 107–121 (1959). doi:10.1021/jc60002a003
- [14] S.G. D'Ávila and R.S. Silva, *J. Chem. Eng. Data* **15**(3), 421–424 (1970).
- [15] K.D. O'Hare and P.L. Spedding, *Chem. Eng. J.* **48**(1), 1–9 (1992). doi:10.1016/0300-9467(92)85001-P
- [16] V. Kokoric, J. Theisen, A. Wilk, C. Penisson, G. Bernard, B. Mizaikoff, and J.C.P. Gabriel, in press.
- [17] I.R. McDonald, *Mol. Phys.* **23**(1), 41–58 (1972). doi:10.1080/00268977200100031
- [18] A.Z. Panagiotopoulos, *Mol. Phys.* **61**(4), 813–826 (1987). doi:10.1080/00268978700101491
- [19] A.Z. Panagiotopoulos, *J. Phys. Condens. Matter* **12**, R25–R52 (2000). doi:10.1088/0953-8984/12/3/201
- [20] A.Z. Panagiotopoulos, *Mol. Phys.* **100**(1), 237–246 (2002). doi:10.1080/00268970110097866
- [21] M. Lísal, W.R. Smith, and I. Nezbeda, *Fluid Phase Equilib.* **181**, 127–146 (2001).
- [22] Y. Luo and B. Roux, *J. Phys. Chem. Lett* **1**(1), 183–189 (2010). doi:10.1021/jz900079w
- [23] M. Kohns, S. Reiser, M. Horsch, and H. Hasse, *J. Chem. Phys.* **144**(8), 084112, (2016). doi: 10.1063/1.4942500
- [24] J.J. Molina, J.F. Dufrêche, M. Salanne, O. Bernard, M. Jardat, and P. Turq, *Phys. Rev. E - Stat. Nonlin Soft Matter Phys.* **80**(6), 065103 (2009). doi:10.1103/PhysRevE.80.065103
- [25] J.J. Molina, J.F. Dufrêche, M. Salanne, O. Bernard, and P. Turq, *J. Chem. Phys.* **135**(23), 234509 (2011). doi:10.1063/1.3668098
- [26] T.N. Nguyen, M. Duvail, A. Villard, J.J. Molina, P. Guilbaud, and J.F. Dufrêche, *J. Chem. Phys.* **142**(2), 024501, (2015). doi: 10.1063/1.4905008
- [27] C. Zhang and X. Yang, *Fluid Phase Equilib.* **231**(1), 1–10 (2005). doi:10.1016/j.fluid.2005.03.018
- [28] S.Y. Noskov, G. Lamoureux, and B. Roux, *J. Phys. Chem. B* **109**(14), 6705–6713 (2005). doi:10.1021/jp045438q
- [29] A. Ghoufi, F. Artzner, and P. Malfreyt, *J. Phys. Chem. B* **120**(4), 793–802 (2016). doi:10.1021/acs.jpcc.5b11776
- [30] M. Bley, M. Duvail, P. Guilbaud, and J.F. Dufrêche, *J. Phys. Chem. B* **121**(41), 9647–9658 (2017). doi:10.1021/acs.jpcc.7b04011
- [31] D.A. Case, V. Babin, J.T. Berryman, R.M. Betz, Q. Cai, D.S. Cerutti, T.E. Cheatham, III, T.A. Darden, R.E. Duke, H. Gohlke, A.W. Goetz, S. Gusarov, N. Homeyer, P. Janowski, J. Kaus, I. Kolossváry, A. Kovalenko, T.S. Lee, S. LeGrand, T. Luchko, R. Luo, B. Madej, K.M. Merz, F. Paesani, D.R. Roe, A. Roitberg, C. Sagui, R. Salomon-Ferrer, G. Seabra, C.L. Simmerling, W. Smith, J. Swails, R.C. Walker, J. Wang, R.M. Wolf, X. Wu, and P.A. Kollman, *Amber 14* (University of California, San Francisco, CA, 2014).
- [32] T. Darden, D. York, and L. Pedersen, *J. Chem. Phys.* **98**(12), 10089–10092 (1993). doi:10.1063/1.464397
- [33] J.W. Caldwell and P.A. Kollman, *J. Phys. Chem.* **99**(16), 6208–6219 (1995). doi:10.1021/j100016a067
- [34] E.C. Meng and P.A. Kollman, *J. Phys. Chem.* **100**(27), 11460–11470 (1996). doi:10.1021/jp9536209
- [35] D.A. Case, T.E. Cheatham, T. Darden, H. Gohlke, R. Luo, K.M. Merz, A. Onufriev, C. Simmerling, B. Wang, and R.J. Woods, *J. Comput. Chem.* **26**(16), 1668–1688 (2005). doi:10.1002/jcc.20290
- [36] C.I. Bayly, P. Cieplak, W.D. Cornell, and P.A. Kollman, *J. Phys. Chem.* **97**, 10269–10280 (1993). doi:10.1021/j100142a004
- [37] W.D. Cornell, P. Cieplak, C.I. Bayly, I.R. Gould, K.M. Merz, D.M. Ferguson, D.C. Spellmeyer, T. Fox, J.W. Caldwell, and P.A. Kollman, *J. Am. Chem. Soc.* **117**(6), 5179–5197 (1995). doi:10.1021/ja00124a002
- [38] I.S. Khattab, F. Bandarkar, M.A.A. Fakhree, and A. Jouyban, *Korean J. Chem. Eng.* **29**(6), 812–817 (2012). doi:10.1007/s11814-011-0239-6

- [39] L. Martínez, R. Andrade, E.G. Birgin, and J.M. Martínez, *J. Comput. Chem.* **30**(13), 2157–2164 (2010).
- [40] H.J.C. Berendsen, J.P.M. Postma, W.F. van Gunsteren, A. DiNola, and J.R. Haak, *J. Chem. Phys.* **81**(8), 3684–3690 (1984). doi:10.1063/1.448118
- [41] R.S. Taylor, L.X. Dang, and B.C. Garrett, *J. Phys. Chem.* **100**(28), 11720–11725 (1996). doi:10.1021/jp960615b
- [42] P.K. Yuet and D. Blankschtein, *J. Phys. Chem. B* **114**(43), 13786–13795 (2010). doi:10.1021/jp1067022
- [43] O. Redlich and A.T. Kister, *Ind. Eng. Chem.* **40**(2), 345–348 (1948). doi:10.1021/ie50458a036
- [44] A.H. Narten and A. Habenschuss, *J. Chem. Phys.* **80**(7), 3387–3391 (1984). doi:10.1063/1.447093
- [45] C.J. Benmore and Y.L. Loh, *J. Chem. Phys.* **112**(13), 5877–5883 (2000). doi:10.1063/1.481160
- [46] R.A. Provencal, R.N. Casaes, K. Roth, J.B. Paul, C.N. Chapo, R.J. Saykally, G.S. Tschumper, and H.F. Schaefer, *J. Phys. Chem. A* **104**(7), 1423–1429 (2000). doi:10.1021/jp9919258
- [47] C.B. Kretschmer and R. Wiebe, *J. Am. Chem. Soc.* **71**(5), 1793–1797 (1949). doi:10.1021/ja01173a076
- [48] R.A. Dawe, D.M.T. Newsham, and S.B. Ng, *J. Chem. Eng. Data* **18**(1), 44–49 (1973). doi:10.1021/je60056a013

Appendix. Variation of the activity

The standard deviation of the time-averaged amount of a compound $\sigma \langle N_{\alpha, i}(x_1) \rangle$ is given by

$$\sigma \langle N_{\alpha, i}(x_1) \rangle = \sqrt{\frac{\int_{t_{\text{Eq}}}^{t_{\text{Tot}}} [N_{\alpha, i}(t, x_1)]^2 dt}{t_{\text{P}}} - \left[\frac{\int_{t_{\text{Eq}}}^{t_{\text{Tot}}} N_{\alpha, i}(t, x_1) dt}{t_{\text{P}}} \right]^2}. \quad (\text{A1})$$

The standard deviation of the vapour phase density $\sigma_{\rho_{\alpha, i}}(x_1)$ is obtained via a propagation of the standard deviation

$$\sigma_{\rho_{\alpha, i}}(x_1) = \frac{d\rho_{\alpha, i}(x_1)}{d\langle N_{\alpha, i}(x_1) \rangle} \sigma \langle N_{\alpha, i}(x_1) \rangle. \quad (\text{A2})$$

The variation of the mean vapour phase density $\sigma_{\bar{\rho}_{\alpha}}(x_1)$ of a species α is given by the arithmetic mean of all j different runs

$$\sigma_{\bar{\rho}_{\alpha}}(x_1) = \frac{\sum_{i=1}^j \sigma_{\rho_{\alpha, i}}(x_1)}{j}. \quad (\text{A3})$$

The standard deviation of the activity in the liquid phase $\sigma_{a_{\alpha}}(x_1)$ depends on two independent variables $\bar{\rho}_{\alpha}(x_1)$ and $\bar{\rho}_{\alpha}^*$ and their standard deviation. Thus, the standard deviation of the activity $\sigma_{a_{\alpha}}(x_1)$ is

$$\begin{aligned} \sigma_{a_{\alpha}}(x_1) &= \frac{da_{\alpha}(x_1)}{d\bar{\rho}_{\alpha}(x_1)} \sigma_{\bar{\rho}_{\alpha}}(x_1) + \frac{da_{\alpha}(x_1)}{d\bar{\rho}_{\alpha}^*} \sigma_{\bar{\rho}_{\alpha}^*} \\ &= \frac{1}{\bar{\rho}_{\alpha}^*} \sigma_{\bar{\rho}_{\alpha}}(x_1) + \frac{\bar{\rho}_{\alpha}(x_1)}{(\bar{\rho}_{\alpha}^*)^2} \sigma_{\bar{\rho}_{\alpha}^*}. \end{aligned} \quad (\text{A4})$$